Computers and Structures 296 (2024) 107299

Contents lists available at ScienceDirect

Computers and Structures

journal homepage: www.elsevier.com/locate/compstruc

Computational simulation and acoustic analysis of two-dimensional nano-waveguides considering second strain gradient effects

Bo Yang [a,b,c], Michele Bacciocchi [d], Nicholas Fantuzzi [a,*], Raimondo Luciano [e], Francesco Fabbrocino [b,*]

[a] Department of Civil, Chemical, Environmental and Materials Engineering, University of Bologna, Viale del Risorgimento 2, 40136 Bologna, Italy
[b] Department of Engineering, Telematic University Pegaso, Centro Direzionale ISOLA F2, 80143 Napoli, Italy
[c] Division of Applied Mechanics, Department of Materials Science and Engineering, Uppsala University, 75103 Uppsala, Sweden
[d] Department of Economics, Sciences and Law, University of San Marino, Via Consiglio dei Sessanta 99, 47891 Dogana, San Marino
[e] Department of Engineering, Parthenope University, Centro Direzionale ISOLA C4, 80133 Napoli, Italy

ARTICLE INFO

Keywords:
Periodic nano-waveguides
Wave propagation
Dispersion relation
Stop band
Second strain gradient elasticity
Parameters sensitivity

ABSTRACT

Exploring the wave propagation in nano-waveguides enables the development of on-chip nano-resonators, leading innovative capabilities that enhance acoustics and micro-mechanics. This paper conducts a numerical investigation into the dynamic properties of periodic nano-waveguides. The Second Strain Gradient (SSG) elasticity, which captures the size effects, is used in the determination of the constitutive relations. The weak form including the element matrices is deduced by the Hamilton's principle. Furthermore, a finite element method, based on the periodic structure theory, is introduced to explore the free wave propagation by solving the eigenvalue problems. The stiffness hardening phenomenon manifested in the dispersion curves, band structures, and energy flow vector fields is discussed. The sensitivity of higher order parameters existing in the SSG theory is analyzed. The numerical investigation for wave propagation in the periodic nano-waveguides through the SSG theory is an innovative work, highlighting the significance of the proposed methodology in explaining the special dynamic characteristics of complex nano-waveguides.

1. Introduction

The investigation for nano-phononic crystals has attracted much attention because of their great potential for improving the development and performance of the wave and energy controlling systems, as well as their wide range of engineering applications, including signal processing, molecular manipulation and sensing. Notably, the excellent acoustic and mechanical characteristics of different periodic nano-waveguides make it a promising material for resonators. The application of different heterogeneous nano-waveguides enables the realization of a phononic crystal with on-chip scale.

The structural properties of nano-waveguides are different from the ones of macro-waveguides due to the existence of the size effects, which can be categorized into three major aspects, namely the large surface-volume ratio [1–3], the non-local interactions [4–6], and the micro-deformations (e.g., micro-rotation and micro-stretch) [7–9]. Because of the presence of size effects, the conventional Classical Theory (CT) of elasticity can no longer adequately account for the wave propagation behavior in nano-waveguides [10,11]. To delve into the size-related properties of nano-waveguides, the application of non-classical elasticity theories within the continuum framework has been proposed, which can be classified into the strain gradient family [12–14], the micro-continuum theory [15,16], the surface elasticity theory [17,18] and the non-local elasticity theory [19–21], where the strain gradient family consists of the First Strain Gradient (SG) theory [22,23], the Second Strain Gradient (SSG) theory [24–27], the couple stress theory [28–30] and the modified couple stress theory [31–33]. Under the framework of the couple stress theory, the strain energy not only encompasses conventional deformations but also considers the gradient of the rotation vector. The modified couple stress theory asserts that the couple stress tensor achieves symmetry by enforcing an equilibrium condition for couples' moments. Additionally, the micro-continuum theory [34] comprises the micro-stretch theory, the micro-polar theory, and the micromorphic theory. The micro-stretch theory incorporates the independent stretch scalar of the micro-material. In the domain of micro-polar theory, the independent rotation scalar is employed to characterize the

* Corresponding authors.
E-mail addresses: nicholas.fantuzzi@unibo.it (N. Fantuzzi), francesco.fabbrocino@unipegaso.it (F. Fabbrocino).

https://doi.org/10.1016/j.compstruc.2024.107299
Received 6 September 2023; Accepted 24 January 2024
Available online 7 February 2024

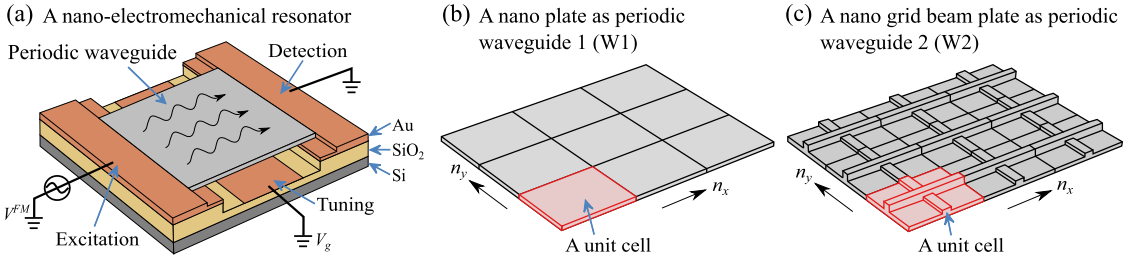

Fig. 1. The design and structure of a nano-electromechanical resonator, which is constructed by electrical excitation port, electrical detection port, electrical tuning and different on chip periodic nano waveguides.

rotational behavior of micro-materials within a structure. Meanwhile, the micro-morphic theory permits the independent rotation and stretch of micro-materials. As suggested by Kroner [35], the stress at a single point within a continuum is influenced by the strains occurring at all points across the body in non-local elasticity theory. A widely accepted model of surface elasticity, as delineated by Gurtin [36], was developed by considering a scalar coefficient representing residual surface tension. The SSG theory was established to provide a comprehensive explanation for the transformation of tension that occurs on a surface of solid plane, by presenting the potential energy as a function of the first, second and third gradient of displacement. The utilization of the SSG theory presents three significant advantages: first, by considering the double stresses and triple stresses, it can eliminate the singularities of physical fields, such as the elastic bend-twist tensor which is singular in the SG theory [37,38]. Second, it allows for the validation of higher order deformations arising from a higher order characteristic length. Last, it demonstrates the occurrence of stiffness hardening resulting from non-local or long-range interactions. Utilizing a third strain gradient theory is unnecessary because, according to the SSG theory, all physical state quantities are smooth and non-singular already.

The above-mentioned theories have garnered widespread attention in the exploration of the properties of nano-sized structures within the framework of analytical and traditional numerical solution. For example, Fantuzzi et al. [39] employed a homogenization technique that is augmented with the micro-polar theory, to determine the constitutive parameters of composite materials. Bacciocchi et al. [40,41] developed a finite element approach to examine the vibratory behavior of laminated plates, incorporating the impact of nonlocal strain gradient phenomenon. Furthermore, Fu et al. [42] conducted a comprehensive investigation of the dynamic characteristics of isotropic materials through the utilization of the analytical strain gradient elasticity. The result is the accurate prediction of the material length-scale parameters. Tuna et al. [43,44] investigated the “explicit” and “implicit” non-local continuum models through the micro-polar theory [43,44]. Their findings indicate that the proposed method serves as a valuable tool for deciphering the mechanical behavior of complex materials. Meanwhile, Tocci Monaco et al. [45] explored the bending behavior of nanoplates under the influence of sinusoidal and uniform loads, using the semi-analytical strain gradient theory. The result displays a good concurrence with the previously literature.

Recently, the Wave Finite Element Method (WFEM) [46] has been proposed as a numerical technique that can be derived from conventional finite element packages, aimed at examining the wave propagation within intricate periodic nano-waveguides. By drawing upon the principles of periodic structure theory [47–49], the representation of the overall periodic structure can be distilled into a single a unit cell, which can reveal the dynamic attributes of the global periodic structure through spectral analysis alone.

This paper introduced several novel contributions. Firstly, the 2D periodic structure technique equipped with the SSG theory was applied to the heterogeneous 2D nano waveguides for the first time to investigate the 2D wave motion. This approach allows for the examination of slowness surfaces, band structure, and energy flow in complex 2D nano waveguides, which has not been explored before. Secondly, the paper enriched the exploration of dynamic properties in nano waveguides. There are more complex waves in realistic structures, including higher order waves. Studying only conventional waves such as bending, tension, and shearing is insufficient to understand the potential dynamic properties of complex nano waveguides. Therefore, investigating multi-mode propagation becomes crucial. Furthermore, the paper presented new insights into stiffness hardening phenomenon and size-dependent characteristics. These properties significantly influence the results but cannot be explained by classical theories. Incorporating size effects and stiffness hardening, induced by higher order parameters, into the WFEM framework offers a novel and valuable approach to effectively study the dynamic properties of nano waveguides. Lastly, the paper integrated the Fourier Amplitude Sensitivity Test (FAST) method with the SSG theory to explore the parameters’ sensitivity for the first time. By doing so, it presented a viable solution for conducting sensitivity analysis on higher order parameters.

The main objectives of this work are, firstly, to confirm the element discretization of complex nano-waveguides through the application of the SSG theory, then to delve into the exploration of wave motion characteristics by employing the WFEM method to solve eigenvalue problems, and ultimately, to illustrate the effect of higher order parameters on wave propagation.

The article is structured as follows: The constitutive relations of the nano-waveguides through the SSG theory and the weak form incorporating the element matrices are introduced in Section 2. In Section 3, the WFEM framework is utilized to solve for free wave propagation, and the sensitivity analysis of higher order parameters is confirmed. Section 4 delves into the wave propagation characteristics and sensitivity analysis. The paper concludes with some conclusions in Section 5.

2. Modeling of nano-waveguides

In this Section, firstly, a nano resonator is introduced as an engineering application and the SSG theory is employed to confirm the matrix form of the strain energy density and the constitutive relations of nano-waveguides in the nano resonator. Subsequently, by applying Hamilton’s principle, the weak form is derived, incorporating the element stiffness and mass matrices.

In order to explore the dynamic properties of nano-waveguides, as shown in Fig. 1, a nano-electromechanical resonator with two different on-chip periodic nano-waveguides is proposed. The intensity at electrical excitation port is modulated at frequency ω, causing a periodic motion. The motion can be detected by monitoring the reflected intensity at electrical detection port. The resonant frequency can be tuned by using a tuning voltage to change the tension of the waveguide. The manufacturing can be realized through the 3D nano-printing technology [50].

2.1. Strain energy density via SSG theory

As introduced by Mindlin in his work on the SSG theory [24], the strain energy density ($\overline{S}$) is a function that is contingent upon the strain

$\boldsymbol{\varepsilon}$, as well as its first and second gradients, namely $\boldsymbol{\varepsilon}_1$ and $\boldsymbol{\varepsilon}_2$, respectively:

$$\overline{S} = \overline{S}(\boldsymbol{\varepsilon}, \boldsymbol{\varepsilon}_1, \boldsymbol{\varepsilon}_2), \tag{1}$$

where $\boldsymbol{\varepsilon} = sym(\nabla \mathbf{W})$, $\boldsymbol{\varepsilon}_1 = \nabla \boldsymbol{\varepsilon}$, and $\boldsymbol{\varepsilon}_2 = \nabla\nabla \boldsymbol{\varepsilon}$, with $\nabla \boldsymbol{\varepsilon} = \nabla\nabla \mathbf{W}$ for Mindlin's form I. Here, ∇ stands for the gradient operator, and $\mathbf{W}$ is the displacement vector. In accordance with the principles of 3D elasticity theory, the displacement vector, as specified within the 3D Cartesian coordinate framework, is given by:

$$\mathbf{W}(x, y, z, t) = \left\{ w_1(x, y, z, t), w_2(x, y, z, t), w_3(x, y, z, t) \right\}^{\top}, \tag{2}$$

in which the displacements along x, y and z are denoted by w_1, w_2, and w_3, respectively.

The $\boldsymbol{\varepsilon}$, $\boldsymbol{\varepsilon}_1$ and $\boldsymbol{\varepsilon}_2$ addressed in the strain energy density can be illustrated by applying the derivatives of the displacement field of first, second, and third order, respectively:

$$\boldsymbol{\varepsilon} = \boldsymbol{\Phi}_1 \mathbf{W},\ \boldsymbol{\varepsilon}_1 = \boldsymbol{\Phi}_2 \mathbf{W},\ \boldsymbol{\varepsilon}_2 = \boldsymbol{\Phi}_3 \mathbf{W}, \tag{3}$$

where $\boldsymbol{\Phi}_1$, $\boldsymbol{\Phi}_2$ and $\boldsymbol{\Phi}_3$ are the operators addressed in Appendix A. Then, the constitutive relations for 3D model based on SSG theory can be established as [51]:

$$\boldsymbol{\tau} = \mathbf{L}\boldsymbol{\varepsilon} + \mathbf{L}_c \boldsymbol{\varepsilon}_2,\ \boldsymbol{\tau}_1 = \mathbf{L}_a \boldsymbol{\varepsilon}_1,\ \boldsymbol{\tau}_2 = \mathbf{L}_b \boldsymbol{\varepsilon}_2 + \mathbf{L}_c^{\top} \boldsymbol{\varepsilon}, \tag{4}$$

in which, $\mathbf{L}_{(6\times6)}$ is the conventional matrix that incorporates the *Lamé* parameters λ and μ related to the Young's modulus E, the Poisson's ratio ν and the shear modulus G, defined as $\lambda = \nu E/(1+\nu)(1-2\nu)$, $\mu = G = E/2(1+\nu)$. $\mathbf{L}_{a(18\times18)}$ is a matrix that includes higher-order parameters $a_{i(i=1,\ldots,5)}$ to characterize the first-order spatial derivatives of the strain tensor. Each a_i is related to $\varepsilon_{1njj}\varepsilon_{1nkk}$, $\varepsilon_{1nnk}\varepsilon_{1kjj}$, $\varepsilon_{1nnk}\varepsilon_{1jjk}$, $\varepsilon_{1njk}\varepsilon_{1njk}$, and $\varepsilon_{1njk}\varepsilon_{1jkn}$, respectively. Furthermore, $\mathbf{L}_{b(30\times30)}$ is a matrix that includes higher-order parameters $b_{i(i=1,\ldots,7)}$ to elucidate the second-order spatial derivatives of the strain tensor. Each b_i is related to $\varepsilon_{2nnjj}\varepsilon_{2kkll}$, $\varepsilon_{2njkk}\varepsilon_{2njll}$, $\varepsilon_{2nnjk}\varepsilon_{2jkll}$, $\varepsilon_{2nnjk}\varepsilon_{2llkj}$, $\varepsilon_{2nnjk}\varepsilon_{2lljk}$, $\varepsilon_{2njkl}\varepsilon_{2njkl}$, and $\varepsilon_{2njkl}\varepsilon_{2jkln}$, respectively. Additionally, $\mathbf{L}_{c(6\times30)}$ is a matrix that includes higher-order parameters $c_{i(i=1,\ldots,3)}$ to incorporates the coupled influence of strain tensor and second-order spatial derivatives of the strain tensor. Each c_i is related to $\varepsilon_{nn}\varepsilon_{2jjkk}$, $\varepsilon_{nj}\varepsilon_{2njkk}$, and $\varepsilon_{nj}\varepsilon_{2kknj}$, respectively. Here, the values of n, j, k and l range from 1 to 3, respectively. The higher order parameters, achieved through the utilization of the inter-atom potential function method, are demonstrated by Shodja [52]. Finally, the expression of the strain energy density within the SSG theory framework can be reformulated in matrix form:

$$\overline{S} = \frac{1}{2}\boldsymbol{\varepsilon}^{\top}\boldsymbol{\tau} + \frac{1}{2}\boldsymbol{\varepsilon}_1^{\top}\boldsymbol{\tau}_1 + \frac{1}{2}\boldsymbol{\varepsilon}_2^{\top}\boldsymbol{\tau}_2. \tag{5}$$

2.2. Weak form derivation

Once the matrix form of the strain energy density is obtained, the weak form will be illustrated. According to the finite element method, the interpolation functions of the hexahedral element can be confirmed by expanding the 1D interpolation functions to 3D. According to the SSG theory, the maximum order of the strain derivatives is two, so the C^2 continuous interpolation functions can be employed to ensure the continuity of the second order derivatives of the strain. Firstly, the interpolation functions of the 1D C^2 continuous along local coordinate $\overline{x}$ are introduced. The six nodal degree of freedoms (DOFs) of 1D element along $\overline{x}$ are expressed as:

$$\begin{aligned}\overline{\mathbf{w}}_1(t) = \Bigg\{ & w_1|_{\overline{x}=-d_e}, \left.\frac{\partial w_1}{\partial \overline{x}}\right|_{\overline{x}=-d_e}, \left.\frac{\partial^2 w_1}{\partial \overline{x}^2}\right|_{\overline{x}=-d_e}, \\ & w_1|_{\overline{x}=d_e}, \left.\frac{\partial w_1}{\partial \overline{x}}\right|_{\overline{x}=d_e}, \left.\frac{\partial^2 w_1}{\partial \overline{x}^2}\right|_{\overline{x}=d_e} \Bigg\}^{\top},\end{aligned} \tag{6}$$

where d_e is the half length of the 1D element. Then, the six-term polynomial function is used to interpolate the 1D scalar field $w_1(\overline{x}, t)$ along $\overline{x}$ direction. This yields:

$$w_1(\overline{x}, t) = \left\{ 1, \overline{x}, \overline{x}^2, \overline{x}^3, \overline{x}^4, \overline{x}^5 \right\} \left\{ \mathrm{h}_0, \mathrm{h}_1, \mathrm{h}_2, \mathrm{h}_3, \mathrm{h}_4, \mathrm{h}_5 \right\}^{\top} = \mathbf{xh}. \tag{7}$$

By incorporating Eq. (7) into Eq. (6), the computation of a 1D nodal displacement vector $\overline{\mathbf{w}}_1(t)$ can be derived as follows:

$$\overline{\mathbf{w}}_1(t) = \left\{ \mathbf{d}_1, \mathbf{d}_2, \mathbf{d}_3, \mathbf{d}_4, \mathbf{d}_5, \mathbf{d}_6 \right\}^{\top} \mathbf{h} = \mathbf{dh}, \tag{8}$$

where $\mathbf{d}_1 = \{1,\ -d_e,\ d_e^2,\ -d_e^3,\ d_e^4,\ -d_e^5\}$, $\mathbf{d}_2 = \{0,\ 1,\ -2d_e,\ 3d_e^2,\ -4d_e^3,\ 5d_e^4\}$, $\mathbf{d}_3 = \{0,\ 0,\ 2,\ -6d_e,\ 12d_e^2,\ -20d_e^3\}$, $\mathbf{d}_4 = \{1,\ d_e,\ d_e^2,\ d_e^3,\ d_e^4,\ d_e^5\}$, $\mathbf{d}_5 = \{0,\ 1,\ 2d_e,\ 3d_e^2,\ 4d_e^3,\ 5d_e^4\}$, $\mathbf{d}_6 = \{0,\ 0,\ 2,\ 6d_e,\ 12d_e^2,\ 20d_e^3\}$.

Then, the displacement vector $w_1(\overline{x}, t)$ along the $\overline{x}$ direction can be represented through the utilization of six quintic Hermite polynomial interpolation functions and the nodal displacement vector, as expressed below:

$$w_1(\overline{x}, t) = \mathbf{x}\mathbf{d}^{-1}\overline{\mathbf{w}}_1(t) = \mathbf{H}(\overline{x})\overline{\mathbf{w}}_1(t), \tag{9}$$

where the interpolation function $\mathbf{H}(\overline{x})$ along $\overline{x}$ direction is introduced as:

$$\mathbf{H}(\overline{x}) = \left\{ \mathrm{H}_1^0(\overline{x}), \mathrm{H}_1^1(\overline{x}), \mathrm{H}_1^2(\overline{x}), \mathrm{H}_2^0(\overline{x}), \mathrm{H}_2^1(\overline{x}), \mathrm{H}_2^2(\overline{x}) \right\}, \tag{10}$$

where $\mathrm{H}_1^0(\overline{x})$, $\mathrm{H}_1^1(\overline{x})$, $\mathrm{H}_1^2(\overline{x})$, $\mathrm{H}_2^0(\overline{x})$, $\mathrm{H}_2^1(\overline{x})$ and $\mathrm{H}_2^2(\overline{x})$ are shown in Appendix B.

On the other hand, the determination of the interpolation functions in both the $\overline{y}$ and $\overline{z}$ directions can be accomplished by: $\mathbf{H}(\overline{y})|_{\overline{y}=\overline{x}} = \{\mathrm{H}_1^0(\overline{y}), \mathrm{H}_1^1(\overline{y}), \mathrm{H}_1^2(\overline{y}), \mathrm{H}_2^0(\overline{y}), \mathrm{H}_2^1(\overline{y}), \mathrm{H}_2^2(\overline{y})\}$, $\mathbf{H}(\overline{z})|_{\overline{z}=\overline{x}} = \{\mathrm{H}_1^0(\overline{z}), \mathrm{H}_1^1(\overline{z}), \mathrm{H}_1^2(\overline{z}), \mathrm{H}_2^0(\overline{z}), \mathrm{H}_2^1(\overline{z}), \mathrm{H}_2^2(\overline{z})\}$.

The representation of $\mathbf{W}(\overline{x}, \overline{y}, \overline{z})$, namely the displacement vector within a 3D hexahedral element, can be facilitated through the utilization of the nodal DOFs $\mathbf{w}(t)$ in conjunction with the interpolation function $\mathbf{H}(\overline{x}, \overline{y}, \overline{z})$:

$$\mathbf{W}(\overline{x}, \overline{y}, \overline{z}, t) = \mathbf{H}(\overline{x}, \overline{y}, \overline{z})\mathbf{w}(t), \tag{11}$$

in which $\mathbf{w} = \{\mathbf{w}_1^{\top}, \mathbf{w}_2^{\top}, \mathbf{w}_3^{\top}\}^{\top}$, $\mathbf{w}_p^{\top} = \{\mathbf{w}_p^{1\top}, \mathbf{w}_p^{2\top}, \ldots, \mathbf{w}_p^{8\top}\}^{\top}$ $(p = 1, 2, 3)$. The interpolation function $\mathbf{H}(\overline{x}, \overline{y}, \overline{z})$ can be deduced by expanding the 1D interpolation functions to 3D:

$$\mathbf{H}(\overline{x}, \overline{y}, \overline{z}) = \{\mathbf{H}_1(\overline{x}, \overline{y}, \overline{z}) \otimes \epsilon_1, \mathbf{H}_2(\overline{x}, \overline{y}, \overline{z}) \otimes \epsilon_2, \mathbf{H}_3(\overline{x}, \overline{y}, \overline{z}) \otimes \epsilon_3\}^{\top}, \tag{12}$$

in which the components within $\mathbf{H}_p(\overline{x}, \overline{y}, \overline{z})$ and $\boldsymbol{\epsilon}_p$ can be denoted as:

$$\mathrm{H}_p^{i(l,m,n)}(\overline{x}, \overline{y}, \overline{z}) = \mathrm{H}_{i'}^{l}(\overline{x})\mathrm{H}_{i''}^{m}(\overline{y})\mathrm{H}_{i'''}^{n}(\overline{z}),\ \boldsymbol{\epsilon}_p = \{\epsilon_{p1}, \epsilon_{p2}, \epsilon_{p3}\}, \tag{13}$$

where $p = 1, 2, 3$. $q = 1, 2, 3$. $i = 1, \ldots, 8$. $l, m, n = 0, 1, 2$. i', i'' and i''' takes 1 and 2 respectively. After the calculation of interpolation functions, the exploration of the element matrices is then proposed through the utilization of the Hamilton's principle:

$$\int_{t_1}^{t_2} (\delta\mathcal{V} - \delta\mathcal{S} + \delta\mathcal{K})\,\mathrm{d}t, \tag{14}$$

in which the virtual strain potential energy δS can be obtained by integrating the strain energy density across its volume:

$$\delta\mathcal{S} = \int_V \delta\overline{S}\mathrm{d}V = \frac{1}{2}\delta\mathbf{w}^{\top}\mathbf{K}\mathbf{w}, \tag{15}$$

where $\mathbf{K}$, as the element stiffness matrix, is expressed as:

$$\begin{aligned}\mathbf{K} = \int_V \big(& \mathbf{H}^{\top}\boldsymbol{\Phi}_1^{\top}\mathbf{L}\boldsymbol{\Phi}_1\mathbf{H} + \mathbf{H}^{\top}\boldsymbol{\Phi}_2^{\top}\mathbf{L}_a\boldsymbol{\Phi}_2\mathbf{H} + \mathbf{H}^{\top}\boldsymbol{\Phi}_3^{\top}\mathbf{L}_b\boldsymbol{\Phi}_3\mathbf{H} \\ & + 2\mathbf{H}^{\top}\boldsymbol{\Phi}_1^{\top}\mathbf{L}_c\boldsymbol{\Phi}_3\mathbf{H}\big)\mathrm{d}V.\end{aligned} \tag{16}$$

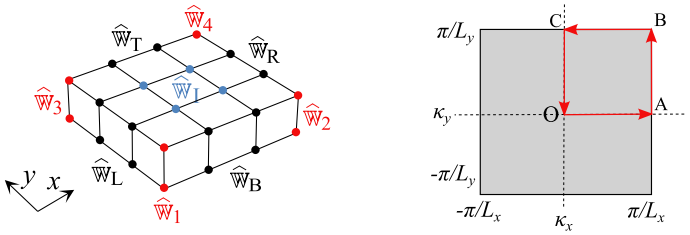

(a) A 2D unit cell. (b) The first Brillouin zone.

Fig. 2. Illustration of the 2D periodic waveguide unit cell and the first Brillouin zone. $\hat{\mathbb{W}}$ means the amplitudes of the displacement, subscript L, R, B, T and I denote left, right, bottom, top boundary and internal DOFs. L_x is the unit cell length along the x, and L_y is the unit cell length along the y.

Meanwhile, the expression for virtual kinetic energy $\delta\mathcal{K}$, which comprises both classical and non-classical components, is manifested as follows [53]:

$$\delta\mathcal{K} = \frac{1}{2}\rho\int_{\Omega}\left[\left(\frac{\partial\delta\mathbf{W}}{\partial t}\right)^{\top}\frac{\partial\mathbf{W}}{\partial t} + l_1^2\left(\frac{\partial^2\delta\mathbf{W}}{\partial x\partial t}\right)^{\top}\frac{\partial^2\mathbf{W}}{\partial x\partial t} + l_2^4\left(\frac{\partial^3\delta\mathbf{W}}{\partial x^2\partial t}\right)^{\top}\frac{\partial^3\mathbf{W}}{\partial x^2\partial t}\right]\mathrm{d}\Omega, \tag{17}$$

where ρ is the linear mass density, l_1 and l_2 denote the higher-order length-scale parameters. Here, it is assumed that the micro-inertia associated with the non-classical component in virtual kinetic energy is disregarded for two reasons: Firstly, as postulated by Mindlin's SSG theory, the mass is divided into two parts within the micro-structure. The first part originates from the macro-material per unit volume, constituting the majority. The second part arises from micro-material per unit volume, representing a minute proportion. In SSG theory, the primary influence on the mechanical properties of the micro-structure is attributed to the higher-order strain terms in the strain energy density and macro-inertia per unit volume. The impact of micro-inertia becomes prominent at high frequencies [54], but its proportion is secondary when compared to the influence of macro-inertia. Secondly, the material employed in this study is pure Aluminum with large identical crystal grains. There is an absence of other micro-materials within the crystal. Consequently, the micro-inertia stemming from micro-material is disregarded in this work. This yields:

$$\delta\mathcal{K} = \frac{1}{2}\rho\int_{V}\left(\frac{\partial\delta\mathbf{W}}{\partial t}\right)^{\top}\frac{\partial\mathbf{W}}{\partial t}\mathrm{d}V = \frac{1}{2}\left(\frac{\partial\delta\mathbf{w}}{\partial t}\right)^{\top}\mathbf{M}\frac{\partial\mathbf{w}}{\partial t}, \tag{18}$$

in which the mass matrix $\mathbf{M}$ is written as:

$$\mathbf{M} = \int_{V}\mathbf{H}^{\top}\rho\mathbf{H}\mathrm{d}V. \tag{19}$$

Furthermore, the expression for virtual work $\delta\mathcal{V}$ performed by external forces can be represented as:

$$\delta\mathcal{V} = \int_{A}\delta\mathbf{W}^{\top}\mathbf{f}_A\mathrm{d}A + \int_{V}\delta\mathbf{W}^{\top}\mathbf{f}_V\mathrm{d}V = \delta\mathbf{w}^{\top}\mathbf{F}, \tag{20}$$

in which $\mathbf{f}_A$ represents the face force, $\mathbf{f}_V$ indicates the volume force. The force vector is introduced as follows:

$$\mathbf{F} = \int_{A}\mathbf{H}^{\top}\mathbf{f}_A\mathrm{d}A + \int_{V}\mathbf{H}^{\top}\mathbf{f}_V\mathrm{d}V. \tag{21}$$

3. Wave motion and sensitivity of higher order parameters

3.1. Wave motion investigation

Based on the WFEM, the traditional finite element method is employed for modeling a single unit cell, whose dynamic equilibrium formulation can be written as:

$$\mathbb{D}\hat{\mathbb{W}} = \hat{\mathbb{F}}, \tag{22}$$

where $\mathbb{D} = (1+\mathrm{i}\eta)\mathbb{K} - \omega^2\mathbb{M}$, whereas the unit cell stiffness matrix $\mathbb{K}$ and the unit cell mass matrix $\mathbb{M}$ are both derived from the assembly of individual element stiffness ($\mathbf{K}$) and mass ($\mathbf{M}$) matrices, respectively, η indicates the damping loss factor, the amplitudes $\hat{\mathbb{W}}$ and $\hat{\mathbb{F}}$ of the nodal displacement vector $\mathbb{W}$ and force vector $\mathbb{F}$ are respectively determined. Fig. 2(a) presents the scheme of a 2D periodic unit cell. The nodal DOFs in the unit cell can be expressed as: $\{\hat{\mathbb{W}}_{\mathrm{Bd}}^{\top}, \hat{\mathbb{W}}_{\mathrm{I}}^{\top}\} = \{\hat{\mathbb{W}}_{\mathrm{I}}^{\top}, \hat{\mathbb{W}}_2^{\top}, \hat{\mathbb{W}}_3^{\top}, \hat{\mathbb{W}}_4^{\top}\ \hat{\mathbb{W}}_{\mathrm{L}}^{\top}, \hat{\mathbb{W}}_{\mathrm{B}}^{\top}, \hat{\mathbb{W}}_{\mathrm{R}}^{\top}, \hat{\mathbb{W}}_{\mathrm{T}}^{\top}, \hat{\mathbb{W}}_{\mathrm{I}}^{\top}\}$. Here, it is assumed that $\hat{\mathbb{F}}_{\mathrm{I}} = 0$, which means that the external loads can not influence the internal DOFs [47]. Then, Eq. (22) will be re-written by partitioning the DOFs into boundary (Bd) and internal (I), leading to:

$$\begin{bmatrix}\mathbb{D}_{\mathrm{BdBd}} & \mathbb{D}_{\mathrm{BdI}}\\ \mathbb{D}_{\mathrm{IBd}} & \mathbb{D}_{\mathrm{II}}\end{bmatrix}\begin{Bmatrix}\hat{\mathbb{W}}_{\mathrm{Bd}}\\ \hat{\mathbb{W}}_{\mathrm{I}}\end{Bmatrix} = \begin{Bmatrix}\hat{\mathbb{F}}_{\mathrm{Bd}}\\ \mathbf{0}\end{Bmatrix}. \tag{23}$$

The nodal DOFs can be described by the propagation constants λ_x and λ_y based on the periodic structures theory:

$$\hat{\mathbb{W}}_{\mathrm{Bd}} = \mathbf{T}_{\mathrm{R}}\hat{\mathbb{W}}_{\mathbf{b}}, \tag{24}$$

with

$$\mathbf{T}_{\mathrm{R}} = \begin{bmatrix}\boldsymbol{i}_{\mathrm{s}} & \lambda_x\boldsymbol{i}_{\mathrm{s}} & \lambda_y\boldsymbol{i}_{\mathrm{s}} & \lambda_x\lambda_y\boldsymbol{i}_{\mathrm{s}} & \mathbf{0} & \mathbf{0} & \mathbf{0} & \mathbf{0}\\ \mathbf{0} & \mathbf{0} & \mathbf{0} & \mathbf{0} & \boldsymbol{i}_{\mathrm{sm}} & \mathbf{0} & \lambda_x\boldsymbol{i}_{\mathrm{sm}} & \mathbf{0}\\ \mathbf{0} & \mathbf{0} & \mathbf{0} & \mathbf{0} & \mathbf{0} & \boldsymbol{i}_{\mathrm{sn}} & \mathbf{0} & \lambda_y\boldsymbol{i}_{\mathrm{sn}}\end{bmatrix}^{\top}, \tag{25}$$

where $\hat{\mathbb{W}}_{\mathbf{b}} = \{\hat{\mathbb{W}}_{\mathrm{I}}^{\top}, \hat{\mathbb{W}}_{\mathrm{L}}^{\top}, \hat{\mathbb{W}}_{\mathrm{B}}^{\top}\}^{\top}$, $\lambda_x = e^{-\mathrm{i}\kappa_x L_x}$, $\lambda_y = e^{-\mathrm{i}\kappa_y L_y}$. The identity matrices of size s, sn, and sm are represented as $\boldsymbol{i}_{\mathrm{s}}$, $\boldsymbol{i}_{\mathrm{sn}}$ and $\boldsymbol{i}_{\mathrm{sm}}$, respectively. The variation of wavenumbers κ_x and κ_y within the first Brillouin zone is depicted in Fig. 2(b). On the other hand, the nodal forces can be confirmed as:

$$\mathbf{T}_{\mathrm{L}}\hat{\mathbb{F}}_{\mathrm{Bd}} = \mathbf{0}, \tag{26}$$

with

$$\mathbf{T}_{\mathrm{L}} = \begin{bmatrix}\boldsymbol{i}_{\mathrm{s}} & \lambda_x^{-1}\boldsymbol{i}_{\mathrm{s}} & \lambda_y^{-1}\boldsymbol{i}_{\mathrm{s}} & \lambda_x^{-1}\lambda_y^{-1}\boldsymbol{i}_{\mathrm{s}} & \mathbf{0} & \mathbf{0} & \mathbf{0} & \mathbf{0}\\ \mathbf{0} & \mathbf{0} & \mathbf{0} & \mathbf{0} & \boldsymbol{i}_{\mathrm{sm}} & \mathbf{0} & \lambda_x^{-1}\boldsymbol{i}_{\mathrm{sm}} & \mathbf{0}\\ \mathbf{0} & \mathbf{0} & \mathbf{0} & \mathbf{0} & \mathbf{0} & \boldsymbol{i}_{\mathrm{sn}} & \mathbf{0} & \lambda_y^{-1}\boldsymbol{i}_{\mathrm{sn}}\end{bmatrix}. \tag{27}$$

In order to solve the eigenvalue problems of Eq. (23), the direct form and inverse form solutions are proposed respectively.

Firstly, for the direct form, the frequency ω and one wavenumber are given, the other wavenumber needs to be calculated. The Eq. (23) will be re-expressed after the dynamic condensation:

$$\overline{\mathbb{D}}\hat{\mathbb{W}}_{\mathrm{Bd}} = \hat{\mathbb{F}}_{\mathrm{Bd}}, \tag{28}$$

where the condensation is expressed as: $\overline{\mathbb{D}} = \mathbb{D}_{\mathrm{BdBd}} - \mathbb{D}_{\mathrm{BdI}}\mathbb{D}_{\mathrm{II}}^{-1}\mathbb{D}_{\mathrm{IBd}}$, in which subscript I and Bd are the internal and boundaries DOFs respectively. Submitting Eq. (24) and Eq. (26) into Eq. (28), as a result:

$$\mathbf{T}_{\mathrm{L}}\overline{\mathbb{D}}\mathbf{T}_{\mathrm{R}}\hat{\mathbb{W}}_{\mathbf{b}} = \mathbf{0}. \tag{29}$$

Suppose one of (λ_x, λ_y) is given (in this work λ_y is given as 1). Then, Eq. (29) can be formulated as:

$$\frac{1}{\lambda_x}\left(\lambda_x^2\mathbf{G}+\lambda_x\mathbf{N}+\mathbf{J}\right)\hat{\mathbb{W}}_{\mathbf{b}}=\mathbf{0}, \tag{30}$$

where $\mathbf{G}$, $\mathbf{N}$ and $\mathbf{J}$ are addressed in Appendix C. The linearization outlined below can be employed to solve the quadratic eigenvalue problem expressed in Eq. (30):

$$\begin{bmatrix}-\mathbf{J} & \mathbf{0}\\ \mathbf{0} & \boldsymbol{i}\end{bmatrix}\begin{Bmatrix}\hat{\mathbb{W}}_{\mathbf{b}}\\ \lambda_x\hat{\mathbb{W}}_{\mathbf{b}}\end{Bmatrix}=\lambda_x\begin{bmatrix}\mathbf{N} & \mathbf{G}\\ \boldsymbol{i} & \mathbf{0}\end{bmatrix}\begin{Bmatrix}\hat{\mathbb{W}}_{\mathbf{b}}\\ \lambda_x\hat{\mathbb{W}}_{\mathbf{b}}\end{Bmatrix}, \tag{31}$$

in which $\boldsymbol{i}$ is the identity matrix.

Secondly, for the inverse form, the frequency ω needs to be calculated based on the two given wavenumbers κ_x and κ_y. The nodal DOFs of a unit cell can be represented by the $\hat{\mathbb{W}}_{\mathrm{I}}, \hat{\mathbb{W}}_{\mathrm{L}}, \hat{\mathbb{W}}_{\mathrm{B}}, \hat{\mathbb{W}}_{\mathrm{I}}$, as a result:

$$\{\hat{\mathbb{W}}_{\mathrm{Bd}}^{\top}, \hat{\mathbb{W}}_{\mathrm{I}}^{\top}\}^{\top}=\begin{bmatrix}\mathbf{T}_{\mathrm{R}} & \mathbf{0}\\ \mathbf{0} & \boldsymbol{i}_{\mathrm{I}}\end{bmatrix}\{\hat{\mathbb{W}}_{\mathrm{I}}^{\top}, \hat{\mathbb{W}}_{\mathrm{L}}^{\top}, \hat{\mathbb{W}}_{\mathrm{B}}^{\top}, \hat{\mathbb{W}}_{\mathrm{I}}^{\top}\}^{\top}, \tag{32}$$

where $\boldsymbol{i}_{\mathrm{I}}$ represents the identity matrix of size I. On the other hand, for the nodal forces:

$$\begin{bmatrix}\mathbf{T}_{\mathrm{L}} & \mathbf{0}\\ \mathbf{0} & \boldsymbol{i}_{\mathrm{I}}\end{bmatrix}\begin{Bmatrix}\hat{\mathbb{F}}_{\mathrm{Bd}}\\ \mathbf{0}\end{Bmatrix}=\mathbf{0}. \tag{33}$$

Then, submitting Eq. (32) and Eq. (33) into Eq. (23), the standard, linear eigenvalue problem in ω^2 will be confirmed as:

$$\left(\mathbb{K}^*-\omega^2\mathbb{M}^*\right)\{\hat{\mathbb{W}}_{\mathrm{I}}^{\top}, \hat{\mathbb{W}}_{\mathrm{L}}^{\top}, \hat{\mathbb{W}}_{\mathrm{B}}^{\top}, \hat{\mathbb{W}}_{\mathrm{I}}^{\top}\}^{\top}=\mathbf{0}, \tag{34}$$

with

$$\mathbb{K}^*=(1+i\eta)\begin{bmatrix}\mathbf{T}_{\mathrm{L}} & \mathbf{0}\\ \mathbf{0} & \boldsymbol{i}_{\mathrm{I}}\end{bmatrix}\mathbb{K},\ \mathbb{M}^*=\mathbb{M}\begin{bmatrix}\mathbf{T}_{\mathrm{R}} & \mathbf{0}\\ \mathbf{0} & \boldsymbol{i}_{\mathrm{I}}\end{bmatrix}. \tag{35}$$

3.2. Sensitivity analysis

The properties of nano waveguides based on the SSG theory are different from the ones of macro-level. It is of importance to explore the influence of higher order parameters existing in SSG theory. The Fourier Amplitude Sensitivity Test (FAST) [55] provides an available solution for the sensitivity analysis of higher order parameters. This global sensitivity investigation method, based on variance decomposition, allows for the exploration of the entire design space and the interpretation of the interactions between input parameters.

In order to analyze the sensitivity of input parameters, firstly, a real valued function $Y=f(\mathbf{p})$ with $f:\mathbb{R}^n\rightarrow\mathbb{R}$ is defined, which can map a vector of input parameters $\mathbf{p}=\{p_1,...,p_n\}$. Here, it should be pointed out that the input parameter $\mathbf{p}$ can be expressed as $\mathbf{p}=\{a_i,b_i,c_i\}$, where $a_{i,(i=1,...,5)}, b_{i,(i=1,...,7)}, c_{i,(i=1,...,3)}$ denote higher order parameters in SSG. The output variance $\mathcal{D}(Y)$ can be expressed as the sum of its conditional variances:

$$\mathcal{D}(Y)=\mathcal{D}_0+\sum_{i=1}^{n}\mathcal{D}_i(p_i)+\sum_{i=1}^{n}\sum_{j>i}^{n}\mathcal{D}_{ij}(p_i,p_j)+...+\mathcal{D}_{1,...,n}(p_1,...,p_n). \tag{36}$$

Then, the sensitivity indexes, which quantify the influence of each variable in a system on the outcome, are defined as:

$$\mathrm{SI}(q)=\frac{\mathcal{D}_q}{\mathcal{D}(Y)}, \tag{37}$$

with $q=1,...,n$. However, the calculation of all the sensitivity indexes requires expensive computational effort. The FAST method can provide the most insight into the effect of a parameter by calculating the first-order sensitivity and total sensitivity indexes. Based on the FAST, the discrete sampling vector is given by [56]:

$$p_i=\frac{1}{2}+\frac{1}{\pi}\arcsin(\sin(\omega_i s+\vartheta_i)). \tag{38}$$

Table 1
The set of integer frequencies ω_i consists of 14, 15 and 16 parameters for $U=4$ (n is the number of input parameters).

n	Frequency set
14	{87, 133, 195, 251, 277, 315, 355, 387, 409, 429, 439, 445, 453, 457}
15	{67, 143, 189, 251, 307, 333, 371, 411, 443, 465, 485, 495, 501, 509, 513}
16	{73, 169, 245, 291, 353, 409, 435, 473, 513, 545, 567, 587, 597, 603, 611, 615}

To reduce interference between input samplings, the frequencies ω_i are chosen to be integers. $\vartheta_i\in[0,2\pi]$ are random real numbers. The integer set frequencies $\{\omega_i\}$ is interference free up to order U under the condition:

$$\sum_{i=1}^{n}\upsilon_i\omega_i\neq 0, \tag{39}$$

where $\upsilon_i\in\mathbb{Z}$ and $\sum_{i=1}^{n}|\upsilon_i|<U$, U denotes a parameter at the investigator disposition. A input sampling is illustrated by utilizing samples number $N>2\omega_n+1$ in the $[0,2\pi]$ interval. In [55], the frequencies ω_i for U (usually set as $U=4$) and less than 19 parameters have been given, as shown in Table 1. The total variance $\mathcal{D}(Y)$ can be confirmed by using the Fourier coefficient $\mathcal{F}_{1j}$ and $\mathcal{F}_{2j}$:

$$\mathcal{D}(Y)=2\sum_{j=1}^{(N-1)/2}(\mathcal{F}_{1j}{}^2+\mathcal{F}_{2j}{}^2), \tag{40}$$

with:

$$\begin{aligned}\mathcal{F}_{1j}{}^2&=\frac{1}{2}\int_0^{2\pi}f(p_1,...,p_n)\cos(js)\mathrm{d}s,\\ \mathcal{F}_{2j}{}^2&=\frac{1}{2}\int_0^{2\pi}f(p_1,...,p_n)\sin(js)\mathrm{d}s.\end{aligned} \tag{41}$$

The contribution of input parameter i is estimated by:

$$\mathcal{D}_i=2\sum_{j=1}^{M}(\mathcal{F}_{1j(\omega_i)}{}^2+\mathcal{F}_{2j(\omega_i)}{}^2). \tag{42}$$

As a result, the main effect of input parameter i is confirmed as:

$$\mathrm{ME}(i)=\frac{\mathcal{D}_i}{\mathcal{D}(Y)}. \tag{43}$$

On the other hand, the total sensitivity index (TSI) of higher order input parameter i is then given as:

$$\mathrm{TSI}(i)=1-\frac{\mathcal{D}_{\sim i}}{\mathcal{D}(Y)}, \tag{44}$$

where $\mathcal{D}_{\sim i}$ denotes the partial variance related to all higher order input parameters except i^{th}.

4. Numerical results

As shown in Fig. 3, two different unit cells of periodic nano-waveguides are introduced, whose material is Aluminum (Al) with $L_x=200a_0$, $L_y=160a_0$, $L_z=10a_0$, $L_{x1}=L_x/8$, $L_{y1}=L_y/8$, $L_{z1}=2L_z$, $L_{z2}=L_z$ (the lattice parameter $a_0=4.046\times10^{-10}$ m). $\rho=2700$ (kg/m^3) is the mass density, 70×10^9 (Pa) is Young's modulus. Damping loss factor $\eta=1e^{-4}$. Table 2 presents the higher order parameters associated with Aluminum (Al) [52].

4.1. Dispersion relation

In this part, in order to investigate the wave propagation along the x direction, as shown in Fig. 4, the dispersion relations of two waveguides are illustrated by the WFEM direct form. At low frequency, the red

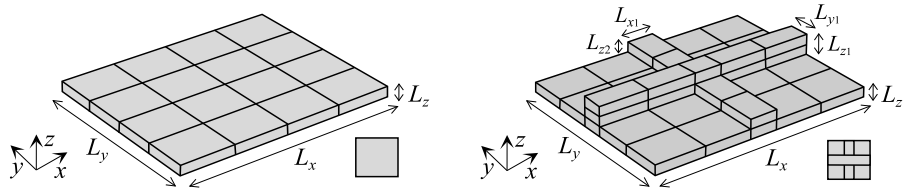

(a) A unit cell in waveguide 1 (W1). (b) A unit cell in waveguide 2 (W2).

Fig. 3. Two different meshed unit cells in periodic nano-waveguides.

Table 2
Higher order parameters a_i, b_i and c_i for material Aluminum. (The unit of a_i and c_i is eV/Å, the unit of b_i is eV·Å. $1eV = 1.602\times10^{-19}$ J, $1Å = 10^{-10}$ m.)

a_1	a_2	a_3	a_4	a_5	b_1	b_2	b_3	b_4	b_5
0.1407	0.0027	-0.0083	0.0966	0.2584	0.7927	0.0644	-0.1943	-0.0009	0.0009
b_6	b_7	c_1	c_2	c_3					
16.1566	48.5291	0.5041	0.3569	0.1782					

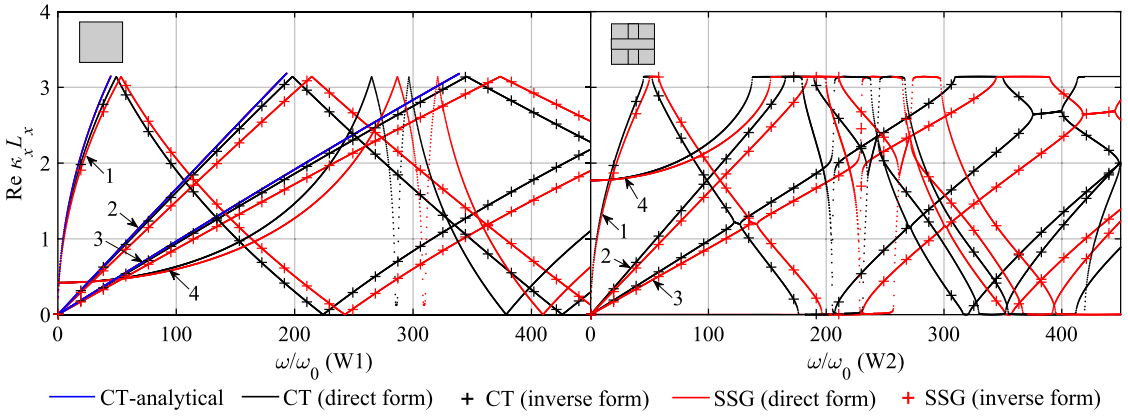

(a) Real part of positive going waves

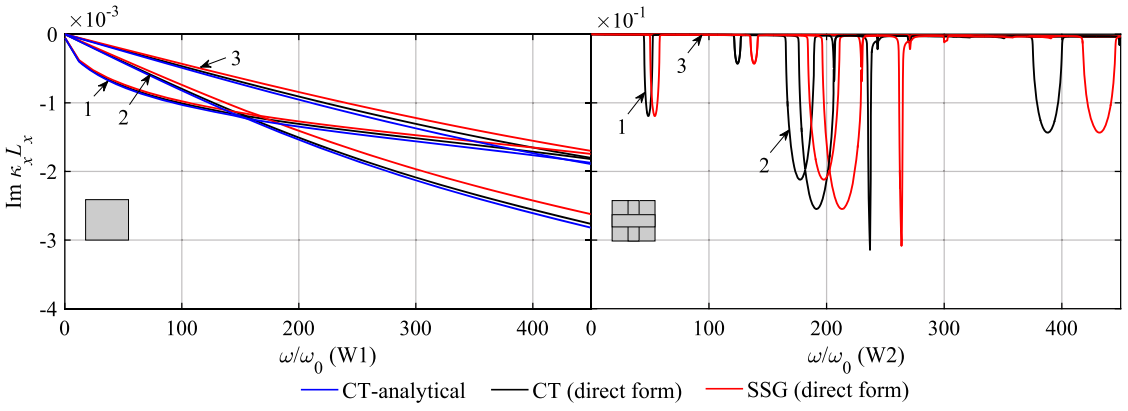

(b) Imaginary part of positive going waves

Fig. 4. Dispersion relations of two waveguides by the WFEM direct form. W1: waveguide 1, W2: waveguide 2. 1: bending, 2: shearing, 3: tension. 4: higher order mode. ω_0 is the first nature frequency of a unit cell.

curves generated via the SSG theory are close to the black curves generated by the CT, however, as the frequency increases, the divergence between them becomes more evident, suggesting that size effects in nano-waveguides become more pronounced. According to the SSG theory, the stiffness hardening phenomenon appears in nano-waveguides at high frequencies due to the presence of non-classical components in SSG, stemming from the non-local interactions between microscopic particles. On the other hand, in order to verify the results of WFEM direct form, the inverse form solution is applied, which can only predict the real parts of the first three modes: bending, shearing and tension. The curves of the first three modes by the inverse form match the ones by the direct form well. At the same time, the tension, shearing, and bending vibration of waveguide 1 are validated by applying the classical analytical methods outlined in [57], showing consistency with the WFEM direct form at the low frequency. Despite the wide use of classical analytical methods, it is not possible to predict high-order modes, such as mode 4. Furthermore, as illustrated in Fig. 4, the wave propagation characteristics of the two waveguides vary. Waveg-

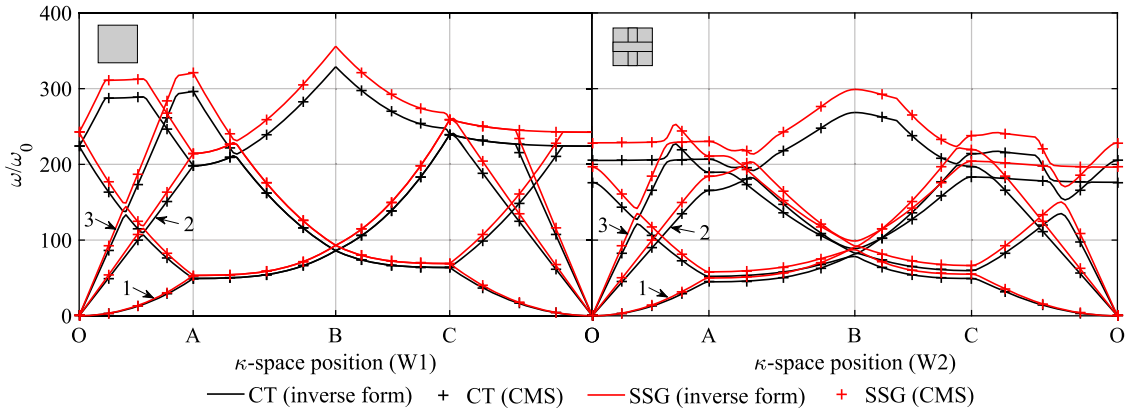

Fig. 5. Band structures of two waveguides by the WFEM inverse form. W1: waveguide 1, W2: waveguide 2. Blue points: the first three modes from the WFEM direct form. 1: bending, 2: shearing, 3: tension.

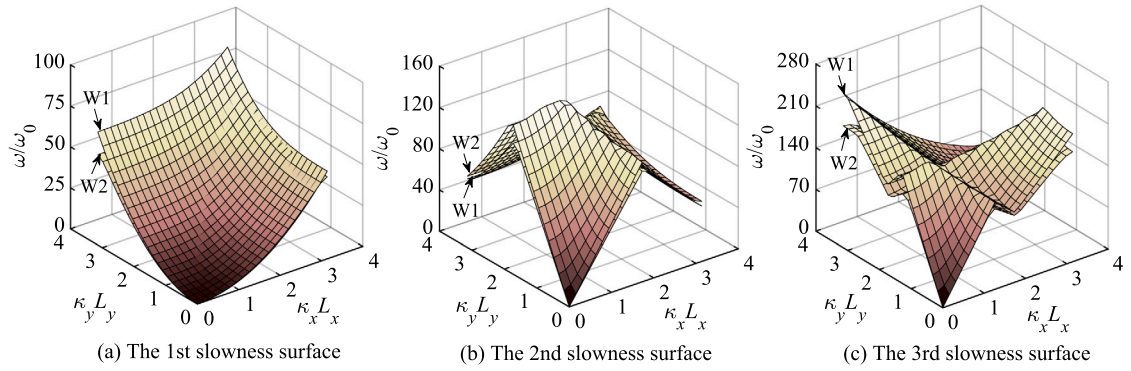

Fig. 6. The first three slowness surfaces of two waveguides in the first quadrant by the SSG. W1: waveguide 1, W2: waveguide 2.

uide 1 does not possess any band gaps, whereas waveguide 2 does, thus providing increased capability for wave or energy control due to the additional beams on the plate. In the context of waveguide 2, the band gap refers to a range of frequencies within which waves cannot propagate through the waveguide. This phenomenon is often associated with periodic structures in waveguides. The physical meaning of the band gap in waveguide 2 is related to the concept of forbidden energy ranges for the guided modes within the waveguide structure. In a periodic waveguide structure, the introduction of periodic variations in the geometry creates a band structure for the guided modes. This band structure consists of allowed and forbidden frequency ranges. The restriction on certain frequencies is a result of constructive and destructive interference within the periodic structure, leading to the formation of a band gap. On the contrary, in waveguide 1 without any periodic structures or variations in material properties, there are no band gaps. The absence of periodicity typically means that the wave can propagate freely, and there are no forbidden frequency ranges for wave propagation. Waveguides without band gaps are still employed in various applications, especially when continuous and broadband transmission of waves is desired.

4.2. Band structures

Next, in order to analyze wave propagation along the x and y directions, the WFEM inverse form is utilized to introduce the band structures of two nano-waveguides. As presented in Fig. 5, a study is conducted of the first five band structure branches along the O-A-B-C-O boundary. Results from the SSG theory are represented by the red lines and those from the CT by the black lines. At low frequencies, the band structure curve from the SSG is similar to that from the CT; however, the discrepancy between the results from the two approaches increases with increasing frequency. The SSG has a greater frequency value than the CT at the same κ-space location due to the special stiffness hardening character of nano-waveguides. So as to verify the results of band structure, a Component Mode Synthesis (CMS) method [58] is applied, which shows a good matching with the WFEM inverse form. Furthermore, in the waveguide 2, there exist visible band gaps between the different branches. For example, at the κ-space position A, the first band gap of mode 1 starts at around $\omega/\omega_0 = 50$ by CT but $\omega/\omega_0 = 55$ by SSG. The first band gap of mode 2 starts at around $\omega/\omega_0 = 160$ by CT but $\omega/\omega_0 = 180$ by SSG. What is more, the first band gap of mode 3 starts at around $\omega/\omega_0 = 300$ by CT but $\omega/\omega_0 = 340$ by SSG. The band gap range is the widest from tension, but the narrowest from bending.

4.3. Slowness surfaces

In this part, the wave propagation in the first Brillouin zone is introduced based on the SSG. The 3D surfaces in Fig. 6 demonstrate a symmetric property with respect to wavenumbers κ_x and κ_y, hence only the first three slowness surfaces of the two waveguides in the first quadrant are calculated. The energy in waveguide 1 is greater than that of waveguide 2 at the same κ-space point, as evidenced by the fact that the first and third slowness surfaces of waveguide 1 are higher than those of waveguide 2. However, the surface position of waveguide 1 is lower than waveguide 2 in the second slowness surfaces, which indicates that the energy in the waveguide 1 is smaller than the energy in the waveguide 2. On the other hand, waveguide 1 has a high capacity for wave propagation and a low capacity for wave control, whereas waveguide 2 has a low capacity for wave propagation and a high capacity for wave control. What is more, the energy across the 1st Brillouin zone of the 1st slowness surface is uniformly distributed. However, on the 2nd and

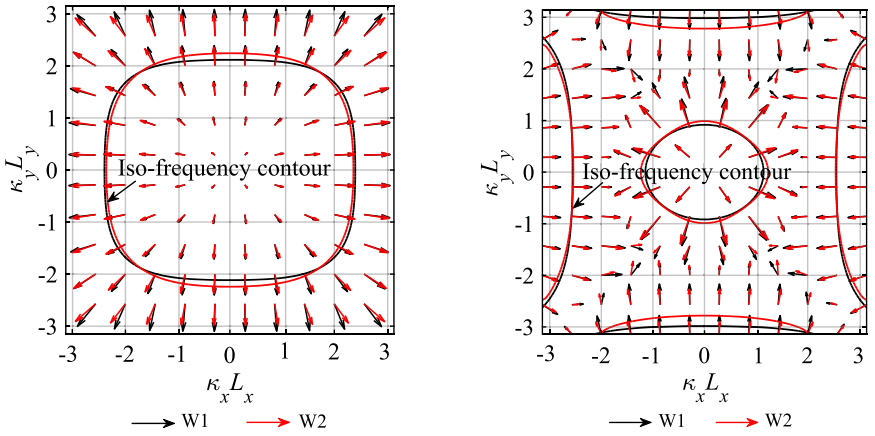

(a) The 1st slowness surface($\omega/\omega_0 = 20$) (b) The 2nd slowness surface($\omega/\omega_0 = 50$)

Fig. 7. The energy flow of the first two slowness surfaces generated by the CT and the SSG. W1: waveguide 1, W2: waveguide 2.

3rd slowness surfaces, the main energy is distributed in some specific regions. For example, most of the energy on the 2nd slowness surface is situated in the center of the first quadrant, while on the 3rd slowness surface, the bulk of the energy is localized at A in the x-direction and C in the y-direction in κ-space.

4.4. Energy flow vector fields

In this part, the SSG and CT are employed to examine the energy flow on the first two slowness surfaces to further investigate the wave propagation in the nano-waveguides, as illustrated in Fig. 7, with arrows denoting the direction and gradient of the energy flow. The iso-frequency contours of the first and second slowness surfaces are selected at ratios of $\omega/\omega_0 = 20$ and $\omega/\omega_0 = 50$, respectively, with respect to the normalized frequency. In the middle of the slowness surface, the arrows by the SSG and the CT almost overlap on the xy plane, which means that the direction and gradient of energy flow projected onto the xy plane by the SSG and CT are basically equivalent at the same κ-space point. However, as the wavenumber increases, the energy direction and gradient by the SSG become different from the ones by CT. The consideration of high-order parameters within the framework of SSG theory, which captures the non-local characteristics, leads a "hardening" of the nano-waveguide, thereby altering wave propagation. Furthermore, on the first slowness surface, the wave outwards in all directions. The iso-frequency contour of the SSG is situated within the CT's contour in the x-axis, yet beyond the CT's contour in the y-axis. On the second slowness surface, the energy propagates outward in the middle, but inward at the edge. At the midpoint of the slowness surface, the iso-frequency contour of the SSG lies outside of the one by the CT, whereas at the edge of the slowness surface, the iso-frequency contour via the SSG is located inside the contour via the CT in the y direction and outside in the x direction.

The harmonic displacement, subject to the Born-von Karman boundary conditions [10,58], are investigated, and it is approximated that the response is unaffected by boundary conditions in damped systems. The conventional FE method expresses the harmonic displacement fields of nano waveguides with 10 unit cells along the x and y directions via the equation $(1 + i\eta')\mathbb{K}_g - \omega^2\mathbb{M}_g]\hat{\mathbb{W}}_g = \hat{\mathbb{F}}_g$ [10], in which $\mathbb{K}_g$ and $\mathbb{M}_g$ are the stiffness and mass matrices of the global structure, respectively. In this work, a harmonic load with unit amplitude is applied at the middle point of the waveguide along the z direction, subject to a free boundary condition, with a loss factor η' equal to 0.5. As presented in Fig. 8, the harmonic displacement response exhibits directional patterns that are consistent with the expectations derived from the energy flow vector fields. Furthermore, the wave propagation range of SSG and CT is the same at low frequency, with the wave propagating in all directions. At high frequency, however, the range of wave propagation by SSG and CT are dissimilar. For example, as presented in Fig. 9, at a normalized frequency of $\omega/\omega_0 = 50$, which is a high frequency, the iso-displacement contours confirmed at $z/z_c = 0.05$ by both CT and SSG show a strong and evident beaming in the x and y directions, with the wave spreading only in those directions. The high-order parameters that capture non-local properties result in a "hardening" phenomenon, leading a reduced wave propagation range for SSG compared to CT in the x direction.

Table 3
Sampling bounds for inputs.

Input factors	Lower bound	Upper bound	Samples
$a_i (i = 1, ..., 5)$	$-100a_i$	$100a_i$	5000
$b_i (i = 1, ..., 7)$	$-100b_i$	$100b_i$	5000
$c_i (i = 1, ..., 3)$	$-100c_i$	$100c_i$	5000

4.5. Sensitivity of higher order parameters

In this part, firstly, the statistics of the output set with inputs for dispersion relation (bending, shearing and tension) of waveguide 1 are discussed. Here, the input parameter $\mathbf{p}$ in Eq. (36) can be expressed as $\mathbf{p} = \{a_i, b_i, c_i\}$, where $a_{i,(i=1,...,5)}, b_{i,(i=1,...,7)}, c_{i,(i=1,...,3)}$ are higher order input parameters existing in the SSG. The sampling bounds for higher order input parameters are addressed in Table 3. The overall influence of 15 higher order parameters is shown in Fig. 10. There are multiple frequency zones that can be discerned. The real part of bending wave, including mean absorption and standard deviations, increases steeply up to $\omega/\omega_0 = 50$, then decreases till to $\omega/\omega_0 = 280$ and increases after $\omega/\omega_0 = 280$ again. The real parts of mean absorption and standard deviations of shearing and tension waves increase up to $\omega/\omega_0 = 230$ and $\omega/\omega_0 = 370$ respectively and then decrease. On the other hand, for all modes (bending, shearing and tension), as frequency increases, the range between +standard deviation and −standard deviation increases continuously. Also, it shows that the 15 higher order parameters have the greatest impact on bending wave, especially at high frequency.

Then, the total sensitivity of each higher order parameter for real part of bending mode in waveguide 1 is discussed. The first set of parameters, denoted as a_i, characterizes the first-order spatial derivatives of the strain tensor, capturing variations in strain across the material. The second set, represented by b_i, elucidates the second-order spatial derivatives of the strain tensor, describing the curvature of the strain field and providing information about how the strain varies spatially. Additionally, the third set of parameters, c_i, incorporates the coupled influence of strain tensor and second-order spatial derivatives of the strain tensor. As shown in Fig. 11(a), for parameters a_i, the sensitivity in-

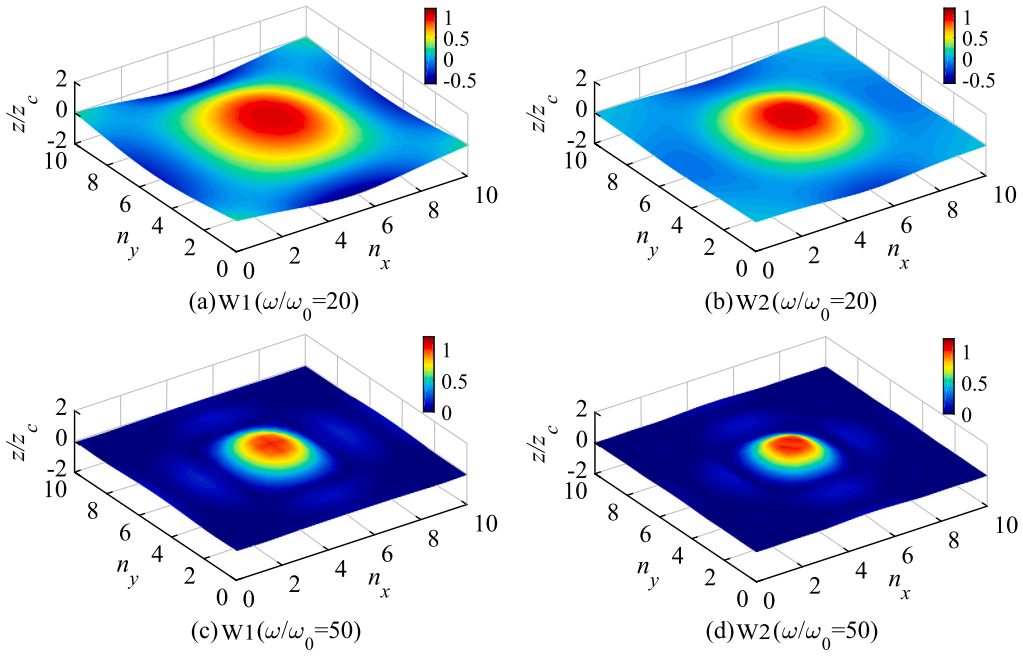

Fig. 8. The harmonic displacement generated by SSG and CT. z_c is the central point amplitude. n_x and n_y are the number of unit cell along x and y direction, respectively. W1: waveguide 1, W2: waveguide 2.

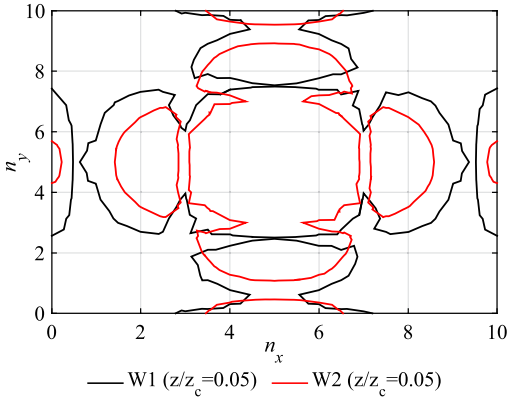

Fig. 9. Normalized forced response contours by SSG and CT. n_x and n_y: unit cell number along x and y direction, respectively. $z/z_c = 0.05$ in which z_c is central point amplitude.

dex of a_2 increases firstly and then decreases with frequency increases. The sensitivity indexes of a_1, a_3, a_4, a_5 decrease with the frequency increases. The parameter a_4 has the biggest influence on the result. For parameters b_i, as illustrated in Fig. 11(b), the sensitivity index of b_7 decreases firstly and then increases with the frequency increases. The sensitivity indexes of b_1, b_2, b_3, b_4, b_5 and b_6 increase with the frequency increases. The parameter b_6 has the biggest influence on the result. Furthermore, as shown in Fig. 11(c), for parameters c_i, the sensitivity indexes of c_1 and c_3 decrease firstly and then increase with the frequency increases. The sensitivity index of c_2 increases with the frequency increases. The parameter c_1 has the biggest influence on the result at low frequency but c_2 has the biggest influence on the result at higher frequency. In general, the sensitivity of higher-order parameters a_i to wave propagation at low frequencies is more pronounced than that at high frequencies. However, the sensitivity of higher-order parameters b_i and c_i to wave propagation at high frequencies is more significant than that at low frequencies. The physical meaning of these higher-order parameters lies in their ability to capture the effects of strain gradients at different orders. Including higher-order terms allows the theory to account for size-dependent material behavior and better describe the mechanical response of materials at small scales or in the presence of microstructures. To validate the outcomes obtained from FAST, the Fourier Amplitude Sensitivity Test with Correlation (FASTC) method [59] is employed. The results obtained from FASTC align with those derived from FAST, affirming the validity of the methodology employed in this study.

5. Conclusions

In this paper, by utilizing the WFEM framework, the SSG theory is applied to analyze the wave propagation in two complex nano-waveguides, which is an original research. The results demonstrate that the proposed method is effective in elucidating the special dynamic features of the periodic nano-waveguides. In order to achieve the numerical modeling, firstly, the constitutive relations of the three-dimensional nano-waveguides are explained through the SSG. The weak form comprising of the element stiffness and mass matrices is studied by applying Hamilton's principle and the corresponding equivalent dynamic equation is derived.

Subsequently, the dispersion relations and band structures for two nano-waveguides are calculated via the WFEM direct form and inverse form, respectively. The result shows that the first three wave modes by the direct form solution confirm the ones by the inverse form. The incorporation of non-classical components into the SSG can result in a stiffness-hardening phenomenon. In the waveguide 1, there is no band gap. But in the waveguide 2, there exist band gaps, which shows a strong wave or energy controlling capacity. At the same time, the harmonic displacement response's directional patterns correlate with the energy flow vector fields' forecasts.

Lastly, the FAST is used to analysis the sensitivity of higher order input parameters on the dispersion relation under the SSG theory. For the statistics of the output set with inputs, the 15 higher order parameters have the greatest impact on bending wave, especially at high frequency. On the other hand, a_4 has the biggest influence on the result among the higher order parameters a_i. b_6 has the biggest influence on the result among the higher order parameters b_i. Furthermore, among the higher order parameters c_i, the parameter c_1 has the biggest influence on the

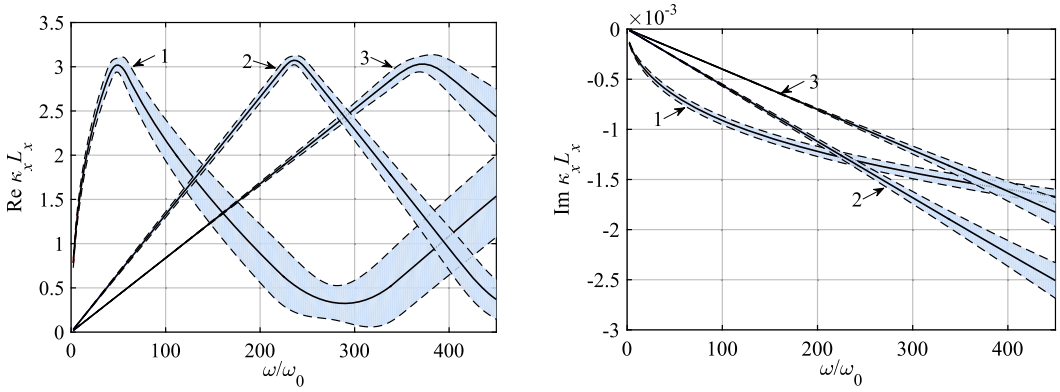

(a) Real part of the positive going bending, tension and shearing waves.

(b) Imaginary part of the positive going bending, tension and shearing waves.

Fig. 10. Mean value ± standard deviation. 1: bending, 2: shearing, 3: tension.

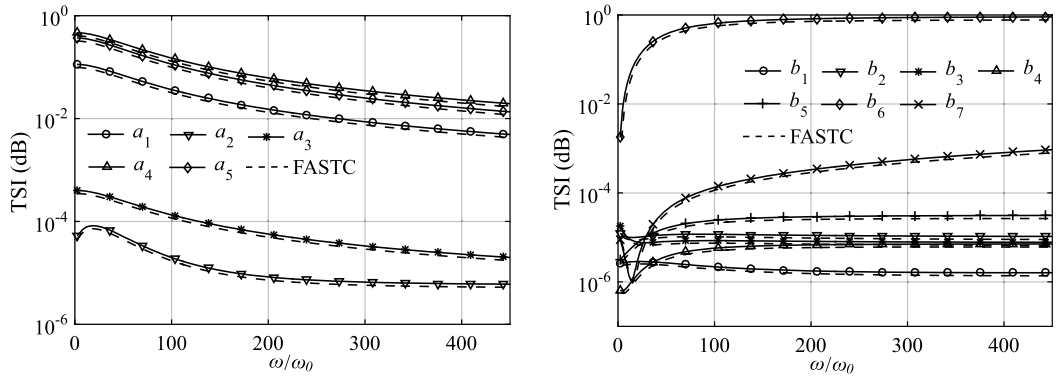

(a) Sensitivity analysis of higher order parameters a_i.

(b) Sensitivity analysis of higher order parameters b_i.

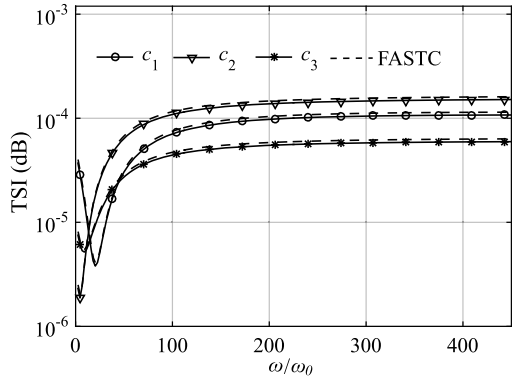

(c) Sensitivity analysis of higher order parameters c_i.

Fig. 11. Total sensitivity indexes of higher order input parameters for bending wave's real part in waveguide 1 through SSG. FASTC: Fourier Amplitude Sensitivity Test with Correlation.

result at low frequency but c_2 has the biggest influence on the result at higher frequency.

CRediT authorship contribution statement

Bo Yang: Conceptualization, Data curation, Formal analysis, Investigation, Methodology, Software, Validation, Writing – original draft, Writing – review & editing. **Michele Bacciocchi:** Supervision, Visualization, Writing – review & editing. **Nicholas Fantuzzi:** Supervision, Visualization, Writing – review & editing. **Raimondo Luciano:** Project administration, Supervision, Visualization, Writing – review & editing. **Francesco Fabbrocino:** Funding acquisition, Project administration, Supervision, Visualization, Writing – review & editing.

Declaration of competing interest

The authors declare that they have no known competing financial interests or personal relationships that could have appeared to influence the work reported in this paper.

Data availability

Data will be made available on request.

Acknowledgements

The authors acknowledge the financial support of the Italian Ministry of University and Research (MUR), Research Grant PRIN 2020 No. 2020EBLPLS on "Opportunities and challenges of nanotechnology in advanced and green construction materials". Additionally, B. Yang acknowledges the financial support by the European Union's Horizon Europe Programme (NANOWAVE) under the Marie Skłodowska-Curie Actions grant agreement No. 101105373.

Appendix A. The matrices $\mathbf{\Phi_1}$, $\mathbf{\Phi_2}$ and $\mathbf{\Phi_3}$ in Eq. (3)

$$\mathbf{\Phi}_1 = \{\boldsymbol{\psi}_1\ \boldsymbol{\psi}_2\ \boldsymbol{\psi}_3\}, \mathbf{\Phi}_2 = \begin{bmatrix} \boldsymbol{\beta}_1 & \mathbf{0} & \mathbf{0} \\ \mathbf{0} & \boldsymbol{\beta}_1 & \mathbf{0} \\ \mathbf{0} & \mathbf{0} & \boldsymbol{\beta}_1 \end{bmatrix} \otimes \boldsymbol{\psi}_4, \mathbf{\Phi}_3 = \begin{bmatrix} \boldsymbol{\beta}_2 & \mathbf{0} & \mathbf{0} \\ \mathbf{0} & \boldsymbol{\beta}_2 & \mathbf{0} \\ \mathbf{0} & \mathbf{0} & \boldsymbol{\beta}_2 \end{bmatrix} \otimes \boldsymbol{\psi}_5$$

where $\otimes$ stands for the Kronecker product. The vectors $\boldsymbol{\beta}_1$ and $\boldsymbol{\beta}_2$ have dimensions 6×1 and 10×1 respectively, with each element having a value of 1. $\boldsymbol{\psi}_1 = \{\partial_x\ 0\ 0\ 0\ \partial_z\ \partial_y\}^\top$, $\boldsymbol{\psi}_2 = \{0\ \partial_y\ 0\ \partial_z\ 0\ \partial_x\}^\top$, $\boldsymbol{\psi}_3 = \{0\ 0\ \partial_z\ \partial_y\ \partial_x\ 0\}^\top$, $\boldsymbol{\psi}_4 = \{\partial_{xx}\ \partial_{yy}\ \partial_{zz}\ 2\partial_{xy}\ 2\partial_{xz}\ 2\partial_{yz}\}^\top$, $\boldsymbol{\psi}_5 = \{\partial_{xxx}\ \partial_{yyy}\ \partial_{zzz}\ 3\partial_{xxy}\ 3\partial_{xxz}\ 3\partial_{yyx}\ 3\partial_{yyz}\ 3\partial_{zzx}\ 3\partial_{zzy}\ 6\partial_{xyz}\}^\top$.

Appendix B. Definition of $H_1^0(\overline{x})$, $H_1^1(\overline{x})$, $H_1^2(\overline{x})$, $H_2^0(\overline{x})$, $H_2^1(\overline{x})$ and $H_2^2(\overline{x})$ in Eq. (10)

$H_1^0(\overline{x}) = 5\overline{x}^3/(8d_e^3) - 15\overline{x}/(16d_e) - 3\overline{x}^5/(16d_e^5) + 1/2$, $H_1^1(\overline{x}) = 5d_e/16 - 7\overline{x}/16 - 3\overline{x}^2/(8d_e) + 5\overline{x}^3/(8d_e^2) + \overline{x}^4/(16d_e^3) - 3\overline{x}^5/(16d_e^4)$, $H_1^2(\overline{x}) = d_e^2/16 - d_e\overline{x}/16 - \overline{x}^2/8 + \overline{x}^3/(8d_e) + \overline{x}^4/(16d_e^2) - \overline{x}^5/(16d_e^3)$, $H_2^0(\overline{x}) = 15\overline{x}/(16d_e) - 5\overline{x}^3/(8d_e^3) + 3\overline{x}^5/(16d_e^5) + 1/2$, $H_2^1(\overline{x}) = 3\overline{x}^2/(8d_e) - 7\overline{x}/16 - 5d_e/16 + 5\overline{x}^3/(8d_e^2) - \overline{x}^4/(16d_e^3) - 3\overline{x}^5/(16d_e^4)$, $H_2^2(\overline{x}) = d_e\overline{x}/16 + d_e^2/16 - \overline{x}^2/8 - \overline{x}^3/(8d_e) + \overline{x}^4/(16d_e^2) + \overline{x}^5/(16d_e^3)$.

Appendix C. Expressions of the coefficients G, N and J in Eq. (30)

$$\mathbf{G} = \begin{bmatrix} \mathbf{G}_{11} & \mathbf{G}_{1L} & \mathbf{G}_{1B} \\ \mathbf{G}_{L1} & \mathbf{G}_{LL} & \mathbf{G}_{LB} \\ \mathbf{G}_{B1} & \mathbf{G}_{BL} & \mathbf{G}_{BB} \end{bmatrix}, \mathbf{N} = \begin{bmatrix} \mathbf{N}_{11} & \mathbf{N}_{1L} & \mathbf{N}_{1B} \\ \mathbf{N}_{L1} & \mathbf{N}_{LL} & \mathbf{N}_{LB} \\ \mathbf{N}_{B1} & \mathbf{N}_{BL} & \mathbf{N}_{BB} \end{bmatrix},$$

$$\mathbf{J} = \begin{bmatrix} \mathbf{J}_{11} & \mathbf{J}_{1L} & \mathbf{J}_{1B} \\ \mathbf{J}_{L1} & \mathbf{J}_{LL} & \mathbf{J}_{LB} \\ \mathbf{J}_{B1} & \mathbf{J}_{BL} & \mathbf{J}_{BB} \end{bmatrix},$$

where $\mathbf{G}_{11} = \overline{\mathbb{D}}_{12} + \overline{\mathbb{D}}_{34} + \overline{\mathbb{D}}_{32}\lambda_y^{-1} + \overline{\mathbb{D}}_{14}\lambda_y$, $\mathbf{G}_{1L} = \overline{\mathbb{D}}_{1R} + \overline{\mathbb{D}}_{3R}\lambda_y^{-1}$, $\mathbf{G}_{1B} = \mathbf{0}$, $\mathbf{G}_{L1} = \overline{\mathbb{D}}_{L2} + \overline{\mathbb{D}}_{L4}\lambda_y$, $\mathbf{G}_{LL} = \overline{\mathbb{D}}_{LR}$, $\mathbf{G}_{LB} = \mathbf{0}$, $\mathbf{G}_{B1} = \overline{\mathbb{D}}_{B2} + \overline{\mathbb{D}}_{T4} + \overline{\mathbb{D}}_{T2}\lambda_y^{-1} + \overline{\mathbb{D}}_{B4}\lambda_y$, $\mathbf{G}_{BL} = \overline{\mathbb{D}}_{BR} + \overline{\mathbb{D}}_{TR}\lambda_y^{-1}$, $\mathbf{G}_{BB} = \mathbf{0}$, $\mathbf{N}_{11} = \overline{\mathbb{D}}_{11} + \overline{\mathbb{D}}_{22} + \overline{\mathbb{D}}_{33} + \overline{\mathbb{D}}_{44} + (\overline{\mathbb{D}}_{31} + \overline{\mathbb{D}}_{42})\lambda_y^{-1} + (\overline{\mathbb{D}}_{13} + \overline{\mathbb{D}}_{24})\lambda_y$, $\mathbf{N}_{1L} = \overline{\mathbb{D}}_{1L} + \overline{\mathbb{D}}_{2R} + (\overline{\mathbb{D}}_{3L} + \overline{\mathbb{D}}_{4R})\lambda_y^{-1}$, $\mathbf{N}_{1B} = \overline{\mathbb{D}}_{1B} + \overline{\mathbb{D}}_{3T} + \overline{\mathbb{D}}_{3B}\lambda_y^{-1} + \overline{\mathbb{D}}_{1T}\lambda_y$, $\mathbf{N}_{L1} = \overline{\mathbb{D}}_{L1} + \overline{\mathbb{D}}_{R2} + \overline{\mathbb{D}}_{L3}\lambda_y^{-1} + \overline{\mathbb{D}}_{R4}\lambda_y$, $\mathbf{N}_{LL} = \overline{\mathbb{D}}_{LL} + \overline{\mathbb{D}}_{RR}$, $\mathbf{N}_{LB} = \overline{\mathbb{D}}_{LB} + \overline{\mathbb{D}}_{LT}\lambda_y$, $\mathbf{N}_{B1} = \overline{\mathbb{D}}_{B1} + \overline{\mathbb{D}}_{T3} + \overline{\mathbb{D}}_{T1}\lambda_y^{-1} + \overline{\mathbb{D}}_{B3}\lambda_y$, $\mathbf{N}_{BL} = \overline{\mathbb{D}}_{BL} + \overline{\mathbb{D}}_{TL}\lambda_y^{-1}$, $\mathbf{N}_{BB} = \overline{\mathbb{D}}_{BB} + \overline{\mathbb{D}}_{TT} + \overline{\mathbb{D}}_{TB}\lambda_y^{-1} + \overline{\mathbb{D}}_{BT}\lambda_y$, $\mathbf{J}_{11} = \overline{\mathbb{D}}_{21} + \overline{\mathbb{D}}_{43} + \overline{\mathbb{D}}_{41}\lambda_y^{-1} + \overline{\mathbb{D}}_{23}\lambda_y$, $\mathbf{J}_{1L} = \overline{\mathbb{D}}_{2L} + \overline{\mathbb{D}}_{4L}\lambda_y^{-1}$, $\mathbf{J}_{1B} = \overline{\mathbb{D}}_{2B} + \overline{\mathbb{D}}_{4T} + \overline{\mathbb{D}}_{4B}\lambda_y^{-1} + \overline{\mathbb{D}}_{2T}\lambda_y$, $\mathbf{J}_{L1} = \overline{\mathbb{D}}_{R1} + \overline{\mathbb{D}}_{R3}\lambda_y$, $\mathbf{J}_{LL} = \overline{\mathbb{D}}_{RL}$, $\mathbf{J}_{LB} = \overline{\mathbb{D}}_{RB} + \overline{\mathbb{D}}_{RT}\lambda_y$, $\mathbf{J}_{B1} = \mathbf{0}$, $\mathbf{J}_{BL} = \mathbf{0}$, $\mathbf{J}_{BB} = \mathbf{0}$.

References

[1] Zhang B, Li H, Kong L, Wang J, Shen H. Strain gradient differential quadrature beam finite elements. Comput Struct 2019;218:170–89.
[2] Hamilton J, Wolfer W. Theories of surface elasticity for nanoscale objects. Surf Sci 2009;603(9):1284–91.
[3] Eremeyev VA, Rosi G, Naili S. Transverse surface waves on a cylindrical surface with coating. Int J Eng Sci 2020;147:103188.
[4] Aksencer T, Aydogdu M. Levy type solution method for vibration and buckling of nanoplates using nonlocal elasticity theory. Physica E, Low-Dimens Syst Nanostruct 2011;43(4):954–9.
[5] Barati MR. Vibration analysis of porous fg nanoshells with even and uneven porosity distributions using nonlocal strain gradient elasticity. Acta Mech 2018;229(3):1183–96.
[6] Miller RE, Shenoy VB. Size-dependent elastic properties of nano-sized structural elements. Nanotechnology 2000;11(3):139.
[7] El-Sapa S. Effect of magnetic field on a microstretch fluid drop embedded in an unbounded another microstretch fluid. Eur J Mech B, Fluids 2021;85:169–80.
[8] Chen Y, Lee JD. Determining material constants in micromorphic theory through phonon dispersion relations. Int J Eng Sci 2003;41(8):871–86.
[9] Zeng X, Chen Y, Lee JD. Determining material constants in nonlocal micromorphic theory through phonon dispersion relations. Int J Eng Sci 2006;44(18–19):1334–45.
[10] Langley RS. The response of two-dimensional periodic structures to point harmonic forcing. J Sound Vib 1996;197:447–69.
[11] Eringen AC, Edelen DGB. On nonlocal elasticity. Int J Eng Sci 1972;10:233–48.
[12] Lazar M, Maugin GA, Aifantis EC. Dislocation in second strain gradient elasticity. Int J Solids Struct 2006:1787–817.
[13] Arefi M, Kiani M, Rabczuk T. Application of nonlocal strain gradient theory to size dependent bending analysis of a sandwich porous nanoplate integrated with piezomagnetic face-sheets. Composites, Part B, Eng 2019;168:320–33.
[14] Hosseini SM, Sladek J, Sladek V, Zhang C. Effects of the strain gradients on the band structures of the elastic waves propagating in 1d phononic crystals: an analytical approach. Thin-Walled Struct 2024;194:111316.
[15] Eringen A. Simple microfluids. Int J Eng Sci 1964;2:205–17.
[16] Chen Y-P, Lee JD, Eskandarian A. Atomistic viewpoint of the applicability of microcontinuum theories. Composites, Part B, Eng 2004;41(8):2085–97.
[17] Gurtin ME, Murdoch AI. A continuum theory of elastic material surfaces. Arch Ration Mech Anal 1975;57(4):291–323.
[18] Li L, Lin R, Ng TY. Contribution of nonlocality to surface elasticity. Int J Eng Sci 2020;152:103311.
[19] Polizzotto C. Nonlocal elasticity and related variational principles. Int J Solids Struct 2001;38:7359–80.
[20] Muc A. Non-local approach to free vibrations and buckling problems for cylindrical nano-structures. Compos Struct 2020;250:112541.
[21] Aminipour H, Janghorban M, Li L. Wave dispersion in nonlocal anisotropic macro/nanoplates made of functionally graded materials. Waves Random Complex Media 2021;31(6):1945–89.
[22] Mindlin RD. Micro-structure in linear elasticity. Arch Ration Mech Anal 1964;16:51–78.
[23] Karami B, Janghorban M, Tounsi A. Variational approach for wave dispersion in anisotropic doubly-curved nanoshells based on a new nonlocal strain gradient higher order shell theory. Thin-Walled Struct 2018;129:251–64.
[24] Mindlin RD. Second gradient of strain and surface tension in linear elasticity. Int J Solids Struct 1965:147–438.
[25] Delfani M, Amadeh-Rajiri S. Elastic and plastic fields induced by a screw dislocation in a nanowire within Mindlin's second strain gradient theory. Appl Math Model 2022;109:77–97.
[26] Cordero NM, Forest S, Busso EP. Second strain gradient elasticity of nano-objects. J Mech Phys Solids 2016;97:92–124.
[27] Ojaghnezhad F, Shodja HM. Surface elasticity revisited in the context of second strain gradient theory. Mech Mater 2016;93:220–37.
[28] Fakhrabadi MMS. Prediction of small-scale effects on nonlinear dynamic behaviors of carbon nanotube-based nano-resonators using consistent couple stress theory. Composites, Part B, Eng 2016;88:26–35.
[29] Shodja H, Goodarzi A, Delfani M, Haftbaradaran H. Scattering of an anti-plane shear wave by an embedded cylindrical micro-/nano-fiber within couple stress theory with micro inertia. Int J Solids Struct 2015;58:73–90.
[30] Behrouz SJ, Rahmani O, Hosseini SA. On nonlinear forced vibration of nano cantilever-based biosensor via couple stress theory. Mech Syst Signal Process 2019;128:19–36.
[31] Tan Z-Q, Chen Y-C. Size-dependent electro-thermo-mechanical analysis of multilayer cantilever microactuators by Joule heating using the modified couple stress theory. Composites, Part B, Eng 2019;161:183–9.
[32] Dehrouyeh-Semnani AM, Nikkhah-Bahrami M. The influence of size-dependent shear deformation on mechanical behavior of microstructures-dependent beam based on modified couple stress theory. Compos Struct 2015;123:325–36.
[33] Yu X, Maalla A, Moradi Z. Electroelastic high-order computational continuum strategy for critical voltage and frequency of piezoelectric nems via modified multiphysical couple stress theory. Mech Syst Signal Process 2022;165:108373.
[34] Eringen AC. Linear theory of micropolar elasticity. J Math Mech 1966:909–23.
[35] Kröner E. Elasticity theory of materials with long range cohesive forces. Int J Solids Struct 1967;3(5):731–42.
[36] Gurtin ME, Murdoch AI. Surface stress in solids. Int J Solids Struct 1978;14(6):431–40.
[37] Lazar M, Maugin GA. Nonsingular stress and strain fields of dislocations and disclinations in first strain gradient elasticity. Int J Eng Sci 2005;43(13–14):1157–84.
[38] Lazar M, Maugin GA, Aifantis EC. Dislocations in second strain gradient elasticity. Int J Solids Struct 2006;43(6):1787–817.
[39] Fantuzzi N, Trovalusci P, Luciano R. Material symmetries in homogenized hexagonal-shaped composites as Cosserat continua. Symmetry 2020;12(3):441.

[40] Bacciocchi M, Fantuzzi N, Luciano R, Tarantino AM. Linear eigenvalue analysis of laminated thin plates including the strain gradient effect by means of conforming and nonconforming rectangular finite elements. Comput Struct 2021;257:106676.
[41] Bacciocchi M, Fantuzzi N, Luciano R, Tarantino AM. Finite element solution of vibrations and buckling of laminated thin plates in hygro-thermal environment based on strain gradient theory. Mech Adv Mat Struct 2022:1–14.
[42] Fu G, Zhou S, Qi L. On the strain gradient elasticity theory for isotropic materials. Int J Eng Sci 2020;154:103348.
[43] Tuna M, Leonetti L, Trovalusci P, Kirca M. 'Explicit' and 'implicit' non-local continuous descriptions for a plate with circular inclusion in tension. Meccanica 2020;55(4):927–44.
[44] Tuna M, Trovalusci P. Scale dependent continuum approaches for discontinuous assemblies: 'explicit' and 'implicit' non-local models. Mech Res Commun 2020;103:103461.
[45] Tocci Monaco G, Fantuzzi N, Fabbrocino F, Luciano R. Semi-analytical static analysis of nonlocal strain gradient laminated composite nanoplates in hygrothermal environment. J Braz Soc Mech Sci Eng 2021;43(5):1–20.
[46] Duhamel D, Mace BR, Brennan M. Finite element analysis of the vibrations of waveguides and periodic structures. J Sound Vib 2006;294:205–20.
[47] Mead D. A general theory of harmonic wave propagation in linear periodic systems with multiple coupling. J Sound Vib 1973;27:235–60.
[48] Ma Y, Deng Z. A hybrid symplectic and high-frequency homogenization analysis for the dispersion property of periodic micro-structured thin plate structures. Appl Math Model 2021;93:276–93.
[49] Hosseini SM, Zhang C. Band structure analysis of Green-Naghdi thermoelastic wave propagation in a gpls/cnts-reinforced metamaterial with energy dissipation. Eng Struct 2022;272:114984.
[50] Pan X, Hong X, Xu L, Li Y, Yan M, Mai L. On-chip micro/nano devices for energy conversion and storage. Nano Today 2019;28:100764.
[51] Yang B, Ichchou M, Zine A, Droz C. Multi-mode propagation and diffusion analysis using the three-dimensional second strain gradient elasticity. Mech Syst Signal Process 2023;187:109970. https://doi.org/10.1016/j.ymssp.2022.109970.
[52] Shodja HM, Ahmadpoor F, Tehranchi A. Calculation of the additional constants for fcc materials in second strain gradient elasticity: behavior of a nano-size Bernoulli-Euler beam with surface effects. Appl Mech 2010;72(2):021008.
[53] Khakalo S, Niiranen J. Form ii of Mindlin's second strain gradient theory of elasticity with a simplification: for materials and structures from nano- to macro-scales. Eur J Mech A, Solids 2018;71:292–319.
[54] Balobanov V, Niiranen J. Locking-free variational formulations and isogeometric analysis for the Timoshenko beam models of strain gradient and classical elasticity. Comput Methods Appl Mech Eng 2018;339:137–59.
[55] Schaibly JH, Shuler KE. Study of the sensitivity of coupled reaction systems to uncertainties in rate coefficients. ii. Applications. J Chem Phys 1973;59:3873–8.
[56] Saltelli A, Tarantola S, Chan KPS. A quantitative model-independent method for global sensitivity analysis of model output. Technometrics 1999;41:39–56.
[57] Graff K. Wave motion in elastic solids. London: Oxford University Press; 1991. p. 75–130. Ch. Longitudinal waves in the rods.
[58] Cotoni V, Langley R, Shorter P. A statistical energy analysis subsystem formulation using finite element and periodic structure theory. J Sound Vib 2008;318:1077–108.
[59] Xu C, Gertner GZ. A general first-order global sensitivity analysis method. Reliab Eng Syst Saf 2008;93(7):1060–71.